Solar Energy 202 (2020) 304–315

Contents lists available at ScienceDirect

Solar Energy

journal homepage: www.elsevier.com/locate/solener

# Two stage modelling of solar photovoltaic cells based on $Sb_2S_3$ absorber with three distinct buffer combinations

M.T. Islam, A.K. Thakur*

*Department of Physics, Indian Institute of Technology Patna, Bihta 801103, Patna, India*

ARTICLE INFO

*Keywords:*
Simulation
$Sb_2S_3$ solar cell
Conduction band offset
Work function
Band gap grading

ABSTRACT

Solar cell research has always been an attraction by virtue of its clean and green status. However, to overcome the implications of high cost and moderate efficiency, there has always been fierce competition to search alternative approach for designing efficient solar cells with optimal performance-cost ratio. Recently, antimony sulfide ($Sb_2S_3$) has received substantial attention as an absorber in thin film solar cells due to earth abundance, low cost, non-toxic property and high optical absorption. Still, its performance could not match Si based cells. In this work, we adopted two-stage simulation approach to design $Sb_2S_3$ absorber based heterojunction solar cell to enhance efficiency. Initial simulation for configuration optimization was done considering thickness, defect density, recombination (radiative, Auger) effect, carrier density of the $Sb_2S_3$ absorber layer. Buffer layer thickness and absorption coefficient optimization was taken up. Further, series and shunt resistance of the device as well as conduction band offset (CBO) at absorber/buffer interface was also optimized at initial stage only. In the next level of simulation, efficiency enhancement was achieved by optimizing optimal back contact metal work function, absorber layer band gap grading and temperature. The aforesaid two-stage optimization yielded efficiency ~24.81%, which is higher than conventional thin film solar cell. The optimal solar cell structure configuration, for $Sb_2S_3$ absorber solar cell, suggested a positive CBO of 0.26 eV (e.g.; ZnS buffer layer), a back contact metal work function of 5.1 eV (e.g.; Mo, Au) and band gap grading window ~1.31 to 1.62 eV.

## 1. Introduction

Si is the most preferred material in 'first generation' solar cell with an ultimate power conversion efficiency (PCE) ~26.7% (Green et al., 2019). Though now commercially available, Si based technology still has inherent weakness of low indirect band gap (~1.12 eV) (Tiedje et al., 1984) and lower optical absorption (Green et al., 1984). It is mandating thick absorber layer (~500 μm) (Thali et al., 2019) and hence high production cost. In contrast, inorganic thin film, i.e.; "second generation" solar cell materials like CdTe and CIGS have efficiency 22.1% (Green et al., 2019) and 23.5% (Green et al., 2019) respectively. The lower abundance of In, Ga and Te and inherent toxicity of Cd are the main hindrance in large-scale commercialization of solar photovoltaic (SPV) cells based on these material combinations. Kesterite (e.g. $Cu_2ZnSnS_4$) and perovskite (e.g. $ABO_3$) have recently been proposed and intensively studied as an absorber layer materials for the 'third generation' solar cell. However, PCE of kesterite is unable to overcome the hurdle of 12.6% (Green et al., 2019) efficiency due to its inherent secondary phase, bulk defects, band tailing etc. On the other hand, the toxicity of lead (Pb) and inherent intrinsic instability of perovskites are presently affecting perovskite solar cell technology (Giraldo et al., 2019; R. Wang et al., 2019).

With little modification in structure, proper selection of absorber aimed at band gap tailoring and lattice matching, in recent years, semiconductor materials such as $Sb_2S_3$, $Sb_2Se_3$ and $Sb_2(S_{1-x}Se_x)_3$ have received increasing attention for design and development of a stable planar heterojunction solar cell. Further, they have advantages of abundance in earth crust as element, low annealing temperature ~400 °C (X. Wang et al., 2018), remarkable stability against moisture and temperature (X. Wang et al., 2019), direct band gap, high absorption coefficient (~$10^5$ $cm^{-1}$), non-toxic and p-type conductivity (Kondrotas et al., 2018; Li et al., 2019). In addition, $Sb_2S_3$ and $Sb_2Se_3$ are nearly isomorphous and hence better control of secondary phase is feasible compared to kesterite compound that contain at least four elements. Despite these advantages, very scanty reports on experimental and theoretical aspects of these materials are available in the literature. The reported experimental efficiency for a number of SPV configuration (Table 1) lie in the range of 1.27% − 7.5%.

Even though a number of reports on $Sb_2S_3$ absorber based solar photovoltaic (SPV) cells (Table 1), covering simulation and

* Corresponding author.
*E-mail addresses:* tasirul.pph16@iitp.ac.in (M.T. Islam), akt@iitp.ac.in (A.K. Thakur).

https://doi.org/10.1016/j.solener.2020.03.058
Received 28 December 2019; Received in revised form 3 March 2020; Accepted 17 March 2020

**Table 1**
Survey on $Sb_2S_3$ absorber based solar cell.

| Device Structure | $V_{OC}$ (V) | $J_{SC}$ (mA/cm$^2$) | FF (%) | Eff. (%) | Reference |
|---|---|---|---|---|---|
| **Simulated** | | | | | |
| AZO/ZnO/CdS/$Sb_2S_3$/Au | 1.23 | 20.15 | 83.1 | 20.6 | (Courel et al., 2019) |
| Se grading $Sb_2S_3$ solar cell | 0.935 | 34.38 | | 28.16 | (Vigil et al., 2018) |
| **Experimental** | | | | | |
| FTO/CdS/$Sb_2S_3$/Ag | 0.6 | 6.12 | 35 | 1.27 | (Escorcia-García et al., 2014) |
| FTO/CdS/$Sb_2S_3$/Au | 0.54 | 9.14 | 47.48 | 2.20 | (K. Wang et al., 2018) |
| FTO/$TiO_2$/$Sb_2S_3$/P3HT/Au | 0.616 | 8.12 | 45.9 | 2.3 | (You et al., 2015) |
| FTO/CdS/$Sb_2S_3$/Au | 0.588 | 10.92 | 46.77 | 3.02 | (Chen et al., 2017) |
| ITO/CdS/$Sb_2S_3$/Au | 0.71 | 10.8 | 45.5 | 3.5 | (Yuan et al., 2016) |
| FTO/$TiO_2$/$Sb_2S_3$/Spiro-OmeTAD/Au | 0.632 | 12.93 | 52.43 | 4.3 | (Wang et al., 2017) |
| FTO/$TiO_2$/$Sb_2S_3$/P3HT/Ag | 0.605 | 7.41 | 43.2 | 1.94 | (Kamruzzaman et al., 2016) |
| FTO/$TiO_2$/$Sb_2S_3$/P3HT/Ag | 0.730 | 11 | 50.5 | 4.06 | (Zimmermann et al., 2015) |
| FTO/$TiO_2$/$Sb_2S_3$/P3HT/Au | 0.670 | 14.92 | 58.04 | 5.77 | (Kim et al., 2014) |
| FTO/$TiO_2$/$Sb_2S_3$/PEDOT:PSS/Au | 0.548 | 13.9 | 67.7 | 5.1 | (Gödel et al., 2015) |
| FTO/$TiO_2$/$Sb_2S_3$/PCPDTBT/Au | 0.616 | 15.3 | 65.7 | 6.18 | (Im et al., 2011) |
| FTO/$TiO_2$/$Sb_2S_3$(Se treated)/Au | 0.69 | 15.3 | 51.2 | 5.4 | (Deng et al., 2019) |
| FTO/mesoporous-$TiO_2$/$Sb_2S_3$/PCPDTBT/Au | 0.711 | 16.1 | 65 | 7.5 | (Choi et al., 2014) |

experimental approach have appeared in literature, none of them could address both the materials and design parameter optimization to its state-of-the-art completeness conforming to real time requirements of developing materials selection criteria for creating an optimal device structure. Therefore, the gap between theoretical/simulated prediction for device efficiency and experimentally obtained efficiency is always wider enough. Consequently, experimental validation of simulated prediction always becomes an unrealistic and unpragmatic target instead of becoming a complementary tool. The primary reason, most of the times, can be ascribed to the fact that a simulation work merely covers one or two parameters, either material or design, to predict efficiency. The same is true in most cases in literature reports of Table 1. The unattended issues for optimization, for example, in the case of $Sb_2S_3$ absorber based device structure are; (i) conduction band offset (CBO) at $Sb_2S_3$/buffer layer junction, (ii) interfacial recombination parameter at $Sb_2S_3$/buffer layer junction, (iii) lattice match with buffer layer (CdS, $TiO_2$) at the front contact, (iv) back contact metal work function thus the Schottky barrier height at the back contact $Sb_2S_3$/Au, (v) absorber band gap grading etc. As a results, high diode ideality factor (~2) and large dark current (reverse saturation current) is $10^{-6}$ mA/cm$^2$ exist at junction (Yuan et al., 2017). So, simulation studies of $Sb_2S_3$ single junction solar cell with appropriate buffer layer require a fresh visit and analysis.

In this work, having analyzed the state-of-the-art limitations of the prior work reported in literature so far, we attempted a comprehensive simulation based on experimentally available parameters in the literature database considering all aspects desirable for material and design optimization for optimal performance of the device structure based on low cost, earth abundant and non-toxic material components. Based on experimental parameters reported in literature, a two stage modelling approach for creation of single junction solar cell was taken up using SCAPS-1D simulation tool. It would be fair to mention at this stage that SCAPS-1D simulation tool does not consider crystalline orientation of the material components while formulating junction comprising absorber and buffer layers for solar cell design. Still the predictions for planar and bulk heterojunction solar cell structure using this tools yields result that agrees well with experimental values of efficiency (Table 2). Some recent works on; (a) $CuIn_{1-x}Ga_xSe_2$ (CIGS) absorber (Bauer et al., 2017), (b) Cu(In, Ga)$Se_2$ (CIGS) absorber (Heise et al., 2017), (c) Cu(In, Ga)$Se_2$ (CIGS) absorber (Schleussner et al., 2013), (d) $CH_3NH_3PbI_3$ ($MAPbI_3$) absorber (Ahn and Lee et al., 2016), (e) $Cu_2ZnSn(S, Se)_4$ (CZTSSe) absorber (Wei et al., 2016), (f) CdTe absorber (Lamb et al., 2017) reported in literature have confirmed this validity. So, without any loss of generality, we can use this tool for simulating single junction planar structure for solar photovoltaic (SPV) cells. The $Sb_2S_3$ absorber, used for simulation studies in the present work, is a one dimensional ribbon having crystalline phase orientation (hk1). It is also known as stibnite.

The undertaken simulation work assumes that; (a) band gap asymmetry between absorber and buffer layers ($E_{gbuffer} > E_{gabsorber}$) is essential, (b) band alignment at absorber/buffer junction should have spike to annul the effect of conduction band offset at absorber/buffer junction in order to enhance the performance parameters, (c) appropriate and optimal work function of back contact metal is desirable to ensure Ohmic response instead of Schottky contact at metal/semiconductor junction, (d) band gap profiling in absorber is mandatory to facilitate carrier collection via effective enhancement of diffusion length of charge carriers, (e) two tier modeling, i.e.; two levels (primary and secondary) of simulation, considering all relevant materials and design parameters are essential prior to predicting efficiency and implementing design structure for fabrication (f) to generalize the approach, few case studies (three distinct devices structure with $Sb_2S_3$ as absorber and $TiO_2$, CdS and ZnS as buffer layer in the present studies) need to be analyzed for consistency check and experimental validation.

**Table 2**
Compares between experimental and simulation efficiency.

| Material component parameters from experimental reference | | | | | | | | Efficiency (η) | |
|---|---|---|---|---|---|---|---|---|---|
| Combinations | | Thick-ness (μm) | Band Gap (eV) | Electron affinity (eV) | Carrier density (cm$^{-3}$) | Dielectric permittivity ($\varepsilon_r$) | Series ($R_S$) & shunt ($R_{Sh}$) resistances (Ω) | Expt. | Simul. |
| $Sb_2S_3$/$TiO_2$ | $Sb_2S_3$ | 1.3[a] | 1.7[a] | 3.7[b] | $5.72 \times 10^{15}$[c] | 7.08[c] | $R_S$ = 1 & | 7.5 | 8.63 |
| | $TiO_2$ | 0.07[a] | 3.2[b] | 4.2[b] | $10^{17}$[d] | 32[d] | $R_{Sh}$ = 1 K | | |
| References: a = (Choi et al., 2014); b = (X. Wang et al., 2018; K. Wang et al., 2018); c = (Vigil et al., 2018); d = (Kanoun et al., 2019) | | | | | | | | | |
| $Sb_2S_3$/CdS | $Sb_2S_3$ | 0.7 | 1.7 | 3.7 | $4.7 \times 10^{15}$ | 31 | $R_S$ = 18.5 & | 3.5 | 5.83 |
| | CdS | 0.06 | 2.4 | 3.98 | $10^{17}$ | 9 | $R_{Sh}$ = 315.5 | | |

Reference: (Yuan et al., 2016).

## 2. Simulation methodology

Numerical simulation has been performed using one dimensional solar capacitance simulator (SCAPS-1D) version 3.3.06 (Burgelman et al., 2000; Decock et al., 2012). SCAPS-1D has advantage over other simulation tools because it enables calculation of parameters like band gap, electron affinity, dielectric permittivity, carrier concentration, carrier mobility, absorption coefficient etc. that can be graded further using this tool (Burgelman et al., 2013; Haddout et al., 2019). To explore the influence of one or a few parameters to the solar cell characteristics the batch-setup facility in the SCAPS simulation tool has been used. A brief scheme of simulation methodology is shown below in the operation flow chart.

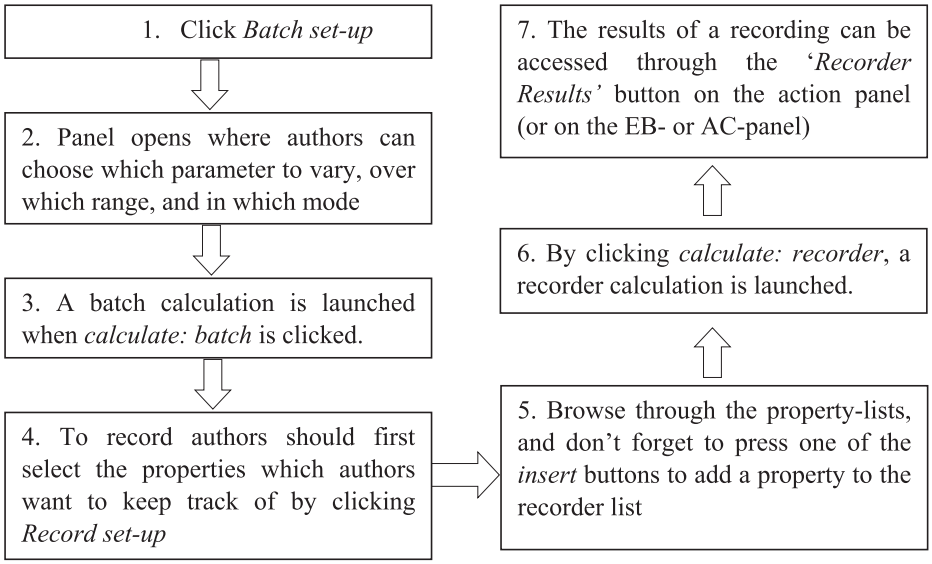


We have performed simulation for the "Back contact/Absorber layer/Buffer layer/Front contact" configuration. Materials physical properties (Table 3) have been taken as input parameters for simulation. The simulation for device design has been carried out for optimization at two levels. In level I optimization, primary focus has been to evaluate and identify the range of desirable parameters such as (a) thickness of the $Sb_2S_3$ absorber layer, (b) thickness and absorption coefficient of the buffer layers (ZnS, CdS, $TiO_2$), (c) defect density, recombination (radiative, Auger) effect, carrier density of the $Sb_2S_3$ absorber layer, (d) series and shunt resistances of the device, (e) conduction band offset (CBO) at absorber/buffer interface. Results after Level I optimization i.e. baselining are compared with experimentally reported efficiency on device structure selected in this work. Still, the simulation was not considered complete even though simulated and experimental efficiency was found little closer in one case ($Sb_2S_3$/$TiO_2$) and just one fourth in the other ($Sb_2S_3$/CdS) selected combination of single junction photovoltaic cell.

So, the second stage (Level II) of the simulation considering back contact metal work function ($\Phi_m$), band gap grading of the absorber layer has been considered. The results obtained after two distinct levels of simulation implementation, has yielded an optimal result in terms of efficiency thereby predicting design parameters for high performance along with developing a criteria for materials selection and design of device structure at the process stage.

## 3. Results and discussion

The central focus of this work is to carry out complete optimization of earth abundant, cheaper material component based solar photovoltaic (SPV) cell. Implementation of a broad based optimization, considering both materials and design parameters has enabled to obtain a set of criteria for real time device design at an optimal efficiency. The two levels of optimization carried out in this work using SCAPS-1D tool is briefly summarized below:

***Level I:*** Initial optimization of desirable parameters such as (a) thickness of the $Sb_2S_3$ absorber layer, (b) thickness and absorption coefficient of the buffer layers (ZnS, CdS, $TiO_2$), (c) defect density, recombination (radiative, Auger) effect, carrier density of the $Sb_2S_3$ absorber layer, (d) series and shunt resistances of the device, (e) conduction band offset at absorber/buffer interface has been done for the baseline configuration of $Sb_2S_3$ absorber based solar cell. This stage is referred to as 'baselining'.

***Level II:*** Enhancement of efficiency by utilizing techniques of (a) work function optimization, (b) band gap grading of the $Sb_2S_3$ absorber layer are performed in Level II. The combination of $Sb_2S_3$/ZnS is having optimal performance among all the absorber/buffer combinations in the level I. So $Sb_2S_3$/ZnS combination is taken up for optimization of efficiency by work function optimization and band gap grading of $Sb_2S_3$ absorber layer. The band gap grading is performed utilizing Se incorporation in $Sb_2S_3$ where with Se incorporation band gap decreases; from $Sb_2S_3$ (1.62 eV) to $Sb_2(S_{1-x}Se_x)_3$ (1.31 eV) (Yang et al., 2015).

### 3.1. Level I optimization – baselining

At this initial stage, parameters optimization with respect to absorber layer thickness, absorption coefficient (α) and thickness of buffer counterpart, radiative recombination coefficient ($cm^3/s$) vis-à-vis absorber thickness, auger recombination current density ($mA/cm^2$) with respect to $Sb_2S_3$ acceptor concentration, defects density of bulk and absorber/buffer interface, series resistance ($R_S$) and shunt resistance ($R_{Sh}$) has been performed for the baseline configuration of $Sb_2S_3$ absorber based solar cell with different buffer layers having wide band gap and n-type carrier density. The electron transition feasibility with respect to $Sb_2S_3$ absorber layer is shown in Fig. 1(a). The proposed device structure is shown in Fig. 1 (b).

#### 3.1.1. Absorber layer thickness optimization vis-à-vis buffer layers

The optimization for the absorber layer thickness, with each buffer (ZnS/CdS/$TiO_2$) combining aimed to achieve an optimal device

**Table 3**
Materials parameters used in the simulation.

| Parameters | $Sb_2S_3$ | $Sb_2Se_3$ | $TiO_2$ | CdS | ZnS |
|---|---|---|---|---|---|
| Thickness (μm) | Variable | Variable | 0.05 | 0.05 | 0.05 |
| Band Gap (eV) | 1.62 (Yang et al., 2015) | 1.08 (Yang et al., 2015) | 3.2 (Kanoun et al., 2019) | 2.4 (Haddout et al., 2019) | 3.6 (Khattak et al., 2018) |
| Electron Affinity (eV) | 3.7 (Vigil et al., 2018) | 3.7 (Vigil et al., 2018) | 4.2 (X. Wang et al., 2018) | 3.9 (X. Wang et al., 2019) | 3.44 (Khattak et al., 2018) |
| Dielectric permittivity ($\varepsilon_r$) | 7.08 (El-Sayad, 2008) | 9.86 (El-Sayad, 2008) | 32 (Kanoun et al., 2019) | 10 (Haddout et al., 2019) | 9 (Khattak et al., 2018) |
| CB effective density of State $N_C$ ($\times 10^{18}$ $cm^{-3}$) | 20 | 18 (Lin et al., 2018) | 10 (Kanoun et al., 2019) | 2.2 (Haddout et al., 2019) | 18 (Khattak et al., 2018) |
| VB effective density of State $N_V$ ($\times 10^{18}$ $cm^{-3}$) | 10 | 2.2 (Lin et al., 2018) | 10 (Kanoun et al., 2019) | 18 (Haddout et al., 2019) | 24 (Khattak et al., 2018) |
| Electron thermal velocity ($cms^{-1}$) | $10^7$ | $10^7$ | $10^7$ | $10^7$ | $10^7$ |
| Hole thermal velocity ($cms^{-1}$) | $10^7$ | $10^7$ | $10^7$ | $10^7$ | $10^7$ |
| Electron mobility ($cm^2$ $V^{-1}$ $s^{-1}$) | 9.8 (Vigil et al., 2018) | 15 (Lin et al., 2018) | 20 (Kanoun et al., 2019) | 50 (Haddout et al., 2019) | 100 (Khattak et al., 2018) |
| Hole mobility ($cm^2$ $V^{-1}$ $s^{-1}$) | 10 (Vigil et al., 2018) | 5.1 (Lin et al., 2018) | 10 (Kanoun et al., 2019) | 5 (Haddout et al., 2019) | 25 (Khattak et al., 2018) |
| Donor/acceptor density, $N_D/N_A$ ($cm^{-3}$) | $5.72 \times 10^{15}$ (Vigil et al., 2018) | $3 \times 10^{13}$ (Lin et al., 2018) | $10^{17}$ (Kanoun et al., 2019) | $10^{18}$ (Haddout et al., 2019) | $4 \times 10^{16}$ (Khattak et al., 2018) |

| Bulk Defects | Density of defects *Nt* ($cm^{-3}$) | Type of Charge state | Capture cross-section ($cm^{-2}$) | | Level above VBM (eV) |
|---|---|---|---|---|---|
| | | | Electron $\sigma_e$ | Hole $\sigma_h$ | |
| $V_S$ | $1 \times 10^{15}$ | (+2/+)/donor (Tumelero et al., 2016) | $10^{-15}$ | $10^{-15}$ | 0.34 (Tumelero et al., 2016) |
| $V_S$ | $1 \times 10^{15}$ | (+/0)/donor | $10^{-15}$ | $10^{-15}$ | 0.43 |
| $Sb_S$ | $1 \times 10^{15}$ | (+/0)/donor | $10^{-15}$ | $10^{-15}$ | 0.28 |
| $Sb_S$ | $1 \times 10^{15}$ | (0/−)/acceptor | $10^{-15}$ | $10^{-15}$ | 0.53 |
| **Interface defects** Interface ($Sb_2S_3$/Buffer) | $1 \times 10^{16}$ | Neutral | $10^{-19}$ | $10^{-19}$ | Uniform Distribution |

| Contact Properties | Front contact | Back contact |
|---|---|---|
| SRV electron ($cms^{-1}$) | $10^7$ | $10^5$ |
| SRV hole ($cms^{-1}$) | $10^5$ | $10^7$ |
| Work Function ($\varnothing_m$) | Flat | Varied (4.6–5.6 eV) |
| Radiative recombination coefficient ($cm^3s^{-1}$)/Auger capture coefficient ($cm^6$ $s^{-1}$) | $2.2 \times 10^{-12}/1 \times 10^{-28}$ (Vigil et al., 2018; Kumar and Thakur, 2018) | |

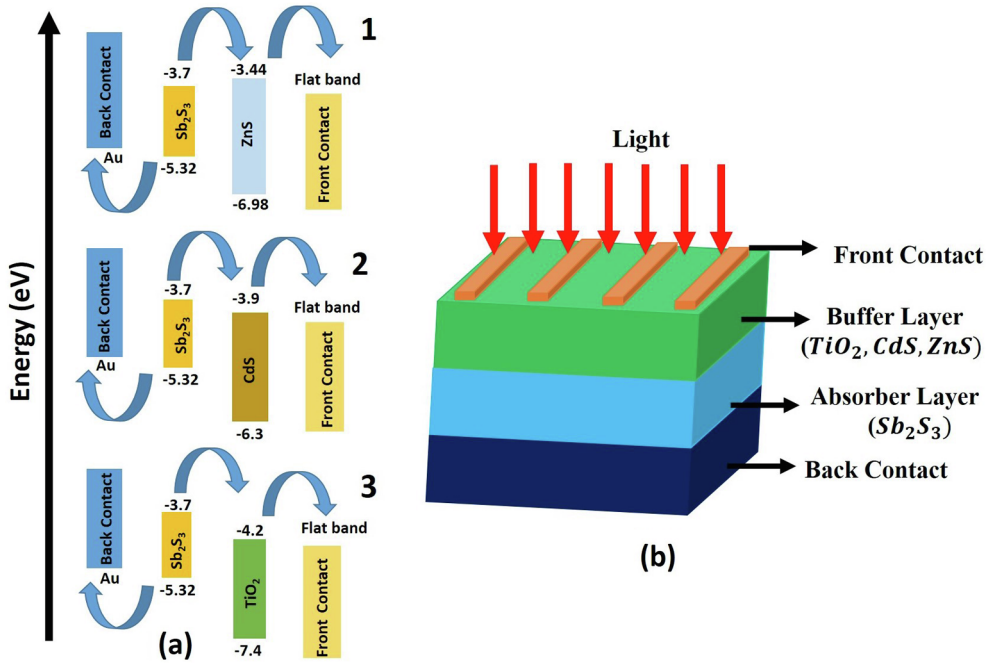


**Fig. 1.** (a) Schematic diagram of the electronic transition feasibility of the expected device. (b) Schematic diagram of the single junction solar device structure "Front contact/buffer counterpart/absorber layer/back contct" used to perform simulation to get output performnace.

structure performance characteristic, estimated in terms of improved open circuit voltage ($V_{OC}$), short circuit current density ($J_{SC}$), fill factor (FF) and efficiency (η), has been obtained. The optimal thickness of the absorber layer is ~1.5–1.8 μm for $Sb_2S_3$/ZnS combination whereas for $Sb_2S_3$/CdS and $Sb_2S_3$/$TiO_2$ combinations, performance parameters attain saturation with absorber thickness window is 2–4 μm. Results are shown in Fig. 2 (a–c). Further, device structure design and material parameters ($V_{OC}$, $J_{SC}$, FF and η) exhibit better match in sulphide buffer (ZnS, CdS) based combination with $Sb_2S_3$ absorber thickness than in oxide ($TiO_2$) based combination in the present studies. However, poor fill factor for $Sb_2S_3$/$TiO_2$ structure is clearly visible among the three under study.

### 3.1.2. Absorber and buffer layer thickness optimization w.r.t. Absorption coefficient (α)

Absorption of solar radiation by device structure holds the key for energy conversion efficiency. Absorber layer and also the buffer layer intrinsic property pertaining to absorption capability play a critical role. Further, solar irradiation absorption by these layers and their thickness determines the separation of electron hole pair produced after absorption of light and also their collection at the respective electrodes. Therefore, optimization for the absorption coefficient and thickness of the absorber and its buffer counterpart is an essential requirement for an efficient device. Uniform absorption coefficient is ~$10^5$ $cm^{-1}$ for the absorber layer at its optimal thickness for each of the device structures, obtained previously in Section 3.1.1 in this work, has been considered as the benchmark for optimizing corresponding buffer layer thickness. Results of the simulation are presented in Fig. 3(a-c). It shows that SPV cell efficiency is strongly dependent on absorption coefficient and thickness of the buffer counterpart. Subsequently, considering a range of absorption coefficient (α) for solar radiation, absorption capability of the buffer layers over a possible range of values vis-à-vis its thickness has been optimized in all the three cases. Results confirm that an optimal thickness of buffer layers 50–90 nm with α ~ $10^4$ –$10^5$ $cm^{-1}$ for ZnS, 50–120 nm with α ~ $10^4$ $cm^{-1}$ for CdS, 50 nm with α ~ $10^4$ $cm^{-1}$ and 50–100 nm with α ~ $10^3$ $cm^{-1}$ for $TiO_2$. Clearly, sulphide based buffer layer such as ZnS & CdS provide adequate flexibility in buffer layer thickness over a high range absorption coefficient. On the other hand, absorption limits are fixed and lower in the case of $TiO_2$ buffer with $Sb_2S_3$ absorber.

### 3.1.3. Radiative recombination coefficient optimization

Recombination is a natural effect and major detriment in the design of an efficient SPV cell. Both the radiative and auger recombination, therefore, need to be at minimal level. Radiative recombination coefficient in the range of $10^{-7}$ to $10^{-15}$ has taken for simulation w.r.t. absorber layer thickness. Fig. 4 (a–c) show that optimal range of radiative recombination coefficient of the order of $10^{-9}$ to $10^{-15}$ yields better efficiency of device structure comprising $Sb_2S_3$ absorber with three different buffer layers. However, η is the best for ZnS and least for $TiO_2$ buffer.

### 3.1.4. Auger recombination optimization

Simulation has been carried out on acceptor concentration of the absorber layer in the range of $10^{10}$ to $10^{17}$ $cm^{-3}$ to evaluate effect on efficiency and auger recombination current density. Results are shown in Fig. 5 (a–c). It is clear that auger recombination current density effect has no role on efficiency at acceptor concentration lower than ~$10^{16}$ $cm^{-3}$. It comes into picture when acceptor concentration is higher than $10^{16}$ $cm^{-3}$.

### 3.1.5. Bulk and interface defect (s) density optimization

Defects in $Sb_2S_3$ is theoretically studied by the (Tumelero et al., 2016). They have reported two types of native point defects which pertaining sulpher vacancies ($V_S$) and antisite defects $Sb_S$ (antimony in a place of a S atom) in the bulk $Sb_2S_3$ absorber with details in the Table 3. If not controlled, these defects act as the recombination centres affecting performance of the device. So, in this simulation study all possible defects are incorporated perhaps for the first time to the best of my knowledge from literature survey. The bulk defects density varied from $10^{10}$ to $10^{17}$ $cm^{-3}$ for optimizing SPV cell performance parameters in each of the three cases in this study. Fig. 6 (a–c) shows that performance parameters are severly affected by defect density beyond its critical limits $10^{15}$ $cm^{-3}$. (Choi et al., 2014) showed that the bulk defects density can achieved of the order of $10^{14}$ $cm^{-3}$ by thioacetamide (TA) treatment. However it is always recommended that bulk

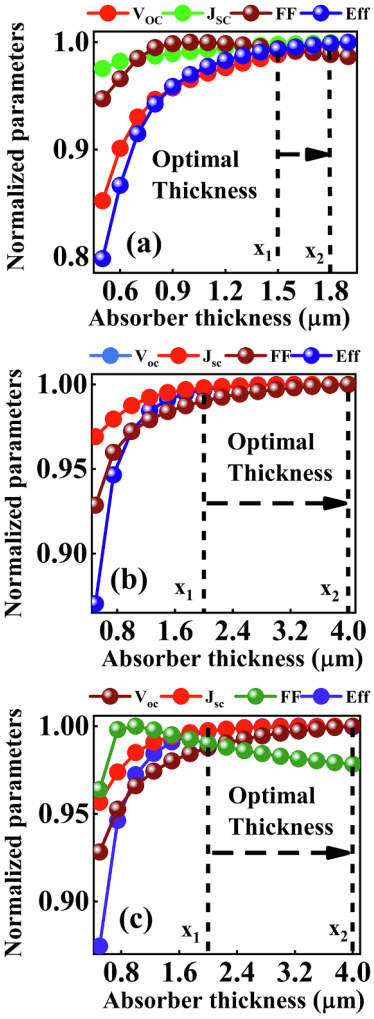


**Fig. 2.** (a–c) Effect of the thickness of the absorber layer on the performance parameters device for $Sb_2S_3$/ZnS, $Sb_2S_3$/CdS and $Sb_2S_3$/$TiO_2$ combination respectively.

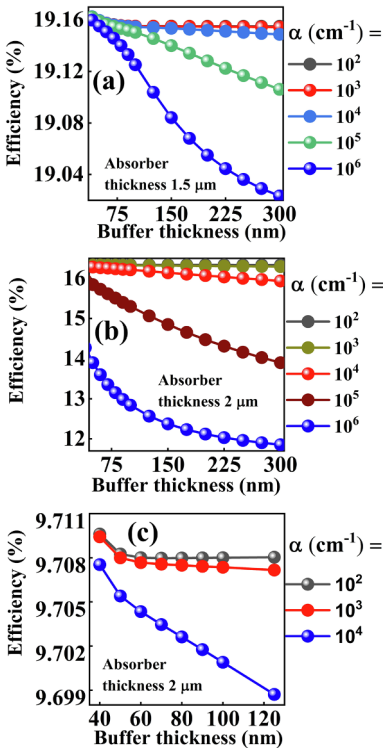


**Fig. 3.** (a–c) Effect of the thickness and absorption coefficient of the buffer layer on the performance parameters of the device for $Sb_2S_3$/ZnS, $Sb_2S_3$/CdS and $Sb_2S_3$/$TiO_2$ combination respectively.

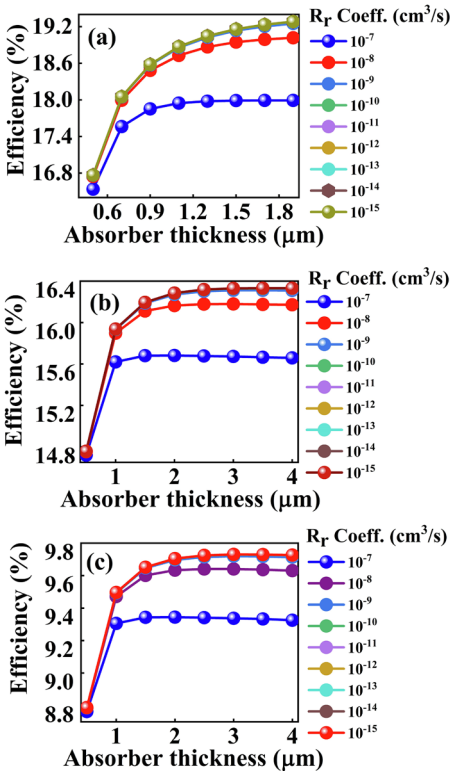


**Fig. 4.** (a–c) Effect of the radiative recombination ($R_r$) coefficient (Coeff.) with respect to absorber layer thickness on the efficiency of the device for $Sb_2S_3$/ZnS, $Sb_2S_3$/CdS and $Sb_2S_3$/$TiO_2$ combination respectively.

defects that also act as trap centres for charge carriers should be much below critical limit. Further, in this simulaiton interface defect density has also been optimized for the three combinations. The optimal estimated interface defect density are $10^{10}$ to $10^{15}$ $cm^{-3}$ with ZnS buffer layer, $10^{10}$ to $10^{13}$ $cm^{-3}$ for CdS and $10^{10}$ to $10^{11}$ $cm^{-3}$ for $TiO_2$ buffer layer respectively. Results are shown in Fig. 7 (a–c). Therefore, ZnS and CdS provide adequate felxibility w.r.t. interface defect density window for $Sb_2S_3$ absorber layer in sharp contrast to that of $TiO_2$.

### *3.1.6. Series and shunt resistance optimization vis-à-vis device performance*

Series and shunt resistance play very significant role on the performance parameters of SPV device. These two parameters, in fact, determine junction characteristics and its implication on performance. At this stage, during simulation, all optimized parameters in the earlier sections such as; absorber and buffer thickness, $Sb_2S_3$ acceptor concentration, buffer donor concentration, bulk defects in absorber material, defects concentration at $Sb_2S_3$/buffer interface etc. were kept fixed at its optimal value. $R_S$ and $R_{Sh}$ were varied in the range of 0–10 Ω $cm^2$ and 100–2000 Ω $cm^2$ respectively during simulation in all the three cases of device structure $Sb_2S_3$/ZnS, $Sb_2S_3$/CdS and $Sb_2S_3$/$TiO_2$ in this study. Results of the optimal series resistance ($R_S$) and shunt resistance

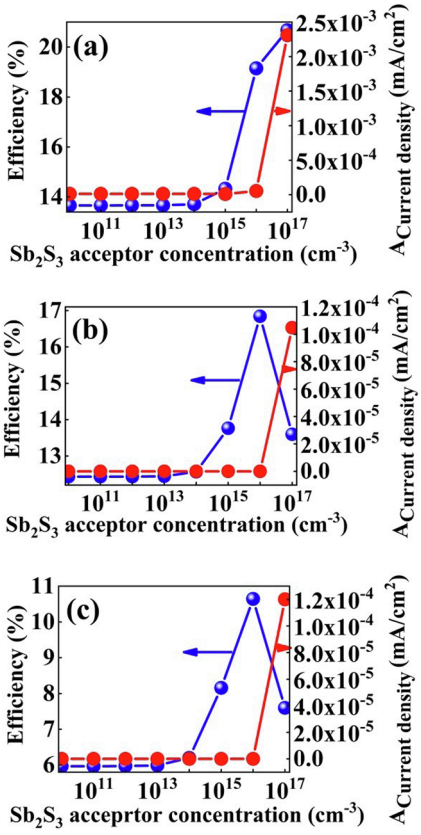


**Fig. 5.** (a–c) Effect of the acceptor concentration on auger recombination ($A_r$) current density and efficiency of the device for $Sb_2S_3$/ZnS, $Sb_2S_3$/CdS and $Sb_2S_3$/$TiO_2$ combination respectively.

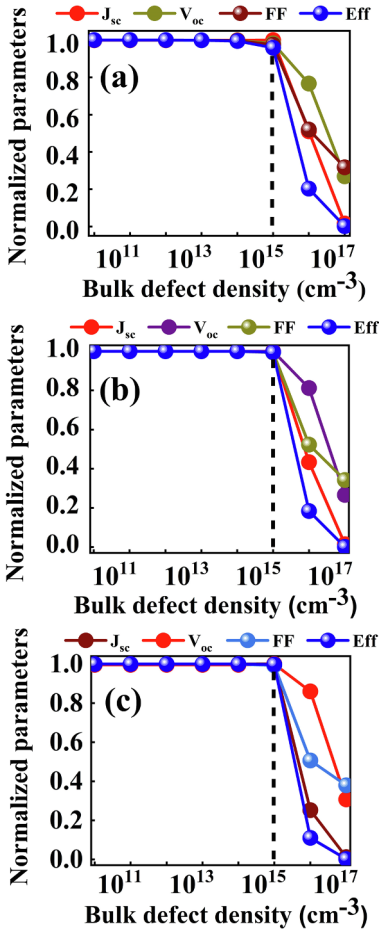


**Fig. 6.** (a–c) Effect of bulk defects density on the performance of the solar device for $Sb_2S_3$/ZnS, $Sb_2S_3$/CdS and $Sb_2S_3$/$TiO_2$ combination respectively.

($R_{Sh}$) values observed as a function of device performance parameters ($V_{OC}$, $J_{SC}$, FF and η) in $Sb_2S_3$/ZnS device structure is presented in the Fig. 8 and for the $Sb_2S_3$/CdS, $Sb_2S_3$/$TiO_2$ device structures (Fig. S1-S2). It is seen that in the case of $Sb_2S_3$/ZnS $V_{OC}$ has very little dependence on series resistance ($R_S$) and $J_{SC}$ has small dependence on the shunt resistance shown in Fig. 8. This behavior is more or less identical in the case of other two structures also (Fig. S1-S2). On the other hand, $R_S$ and $R_{Sh}$ are playing a significant role in limiting the fill factor (FF) values thereby reducing it much below its ideal value of unity. This is shown in the Fig. 8(c). This factor has alone contributed, therefore in lowering the efficiency of $Sb_2S_3$ absorber solar cell structure with all the three buffers to a level much below predicted earlier in literature considering only a few parameters while performing optimization. The results are shown in the Fig. 8 (d) for $Sb_2S_3$/ZnS and in the Fig. S1(d)–S2(d) for $Sb_2S_3$/CdS, $Sb_2S_3$/$TiO_2$ device structures respectively. It is also noted from experimentally reports $R_S$ and $R_{Sh}$ for $Sb_2S_3$ based solar cells are of the order of 6–40 Ω $cm^2$ and 125–856.35 Ω $cm^2$ respectively as reported by (Tamilselvan et al., 2019; K. Wang et al., 2018; Wu et al., 2019). The conventional thin film solar cell like CIGS has $R_S$ and $R_{Sh}$ of the order of 0.17–0.49 Ω $cm^2$ and 880–2710 Ω $cm^2$ respectively (Jackson et al., 2011). In this work, though input values for $R_S$ and $R_{Sh}$ were 1 Ω $cm^2$ and 1000 Ω $cm^2$ employed respectively during simulation, their optimal values came to be 1 Ω $cm^2$ and 1700 Ω $cm^2$ giving thereby an optimized FF ~ 78.69% for $Sb_2S_3$/ZnS.

### 3.1.7. Optimization for conduction band offset at absorber/buffer interface

This optimization is strongly depedent on band alignment between absorber and buffer layer and hence very important for controlled charge flow across junction with adequate control over interfacial recombination. The charge flow through $Sb_2S_3$/buffer junction in SPV depends primarily on the alignment of energy level of the two components. Any mismatch between the energy band in SPV will give rise to a band offset that in turn depend on the difference of ($\chi_{Sb_2S_3} - \chi_{buffer}$) present the conduction band offset ($E_{CBO}$) at the junction, where χ is the electron affinity. There are two types of configurations at the junction one is type-I and other one type-II. In type-I hetero junction the photo-generated electron flow from absorber to buffer layer faces a barrier (or Spike) when ($\chi_{Sb_2S_3} - \chi_{buffer}$) is positive. In contrast, in type-II heterojunction, a cliff will be present at the junction when ($\chi_{Sb_2S_3} - \chi_{buffer}$) is negative. In the present work, conduction band offset (CBO) optimization for all the three device structures comprising $Sb_2S_3$ absorber with buffer layers ZnS, CdS, $TiO_2$ having different electron affinity have been simulated using electron affinity (χ) in Table 3 and keeping all parameters at its optimal level as obtained previously in Sections 3.1.1–3.1.6 for the device. Results on band gap alignment are shown in Fig. 9 (a–c). Presence of negative CBO ~ − 0.5 eV and − 0.2 eV for the $Sb_2S_3$/$TiO_2$ and $Sb_2S_3$/CdS is confirmed by cliff at the respective junctions in the hetero structure (Fig. 9 (b) and (c)). In contrast, a spike ~ + 0.26 eV (positive CBO) appears to $Sb_2S_3$/ZnS heterojunction shown in Fig. 9 (a). An electron affinity of buffer layer lower than of the absorber $Sb_2S_3$ results type-I interface with positive CBO thereby favoring charge flow across junction with adequate control over interfacial recombination. The mechanism related to spike and cliff type CBO affecting SPV cell performance parameters is schematically shown in Fig. 10 (a–b). It is clear that for cliff type CBO, the electron hole recombination is energetically favorable while for spike type CBO it makes difficult for an electron to recombine due to an effective e-h separation. Electron-hole recombination therefore will occur easily for the cliff type CBO compared to spike type CBO due to lower effective separation of the quasi-fermi level for the cliff

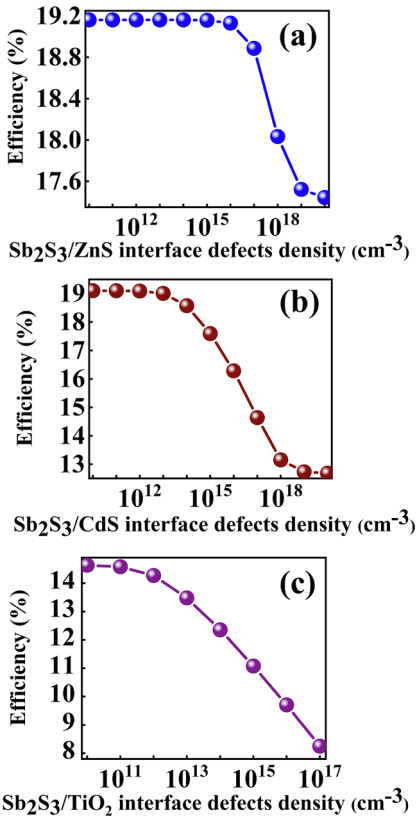


**Fig. 7.** (a–c) Effect of Interface defects density on the efficiency of the solar device for $Sb_2S_3$/ZnS, $Sb_2S_3$/CdS and $Sb_2S_3/TiO_2$ combination respectively.

type CBO resulting in lower $V_{OC}$. Opposed to this, a small value of positive CBO or spike type band alignment will still facilitate transport of photo-generated electrons via tunneling process (Huang et al., 2013). However, mobility of holes is not favored through spiked CBO. A relation between recombination current and CBO is shown in Fig. 10 (c). It is observed that recombination current is lowest for the positive conduction band offset ~0–0.4 eV. This result, therefore, suggests that this range of positive CBO is optimal favoring higher efficiency ~19% in type-I heterojunction with 0.26 eV positive CBO for $Sb_2S_3$/ZnS in the present study. So, for practical applications, ZnS could be a good buffer layer for $Sb_2S_3$ absorber based solar cell provided optimal criteria determined in this study is adopted for practical design. Complete result for all the three device structures in the present study obtained after level I optimization is presented in Table 4.

Further, after level I optimization considering parameters such as; (a) thickness of the $Sb_2S_3$ absorber layer, (b) thickness and absorption coefficient of the buffer layers (ZnS, CdS, $TiO_2$), (c) defect density, recombination (radiative, Auger) effect, carrier density of the $Sb_2S_3$ absorber layer, (d) series and shunt resistances of the device, (e) conduction band offset at absorber/buffer interface, the results (Table 4) so obtained on performance parameters suggest that $Sb_2S_3$/ZnS is the better among all three configurations. It is seen that the efficiency of single junction solar cell based on $Sb_2S_3/TiO_2$ combination approaches close to its experimental reported efficiency (Choi et al., 2014) whereas in the case of $Sb_2S_3$/CdS combination it is nearly one fourth of experimental efficiency (Yuan et al., 2016). Such a difference in simulated and experimental efficiency of $Sb_2S_3$/CdS combination can be attributed to limitations of the experiment that needs to be improved along with improvement in fabrication process at each stage of design implementation. However, no experimental work on $Sb_2S_3$/ZnS combination has yet been taken up. We are working currently on its experimental part also and it will be reported separately.

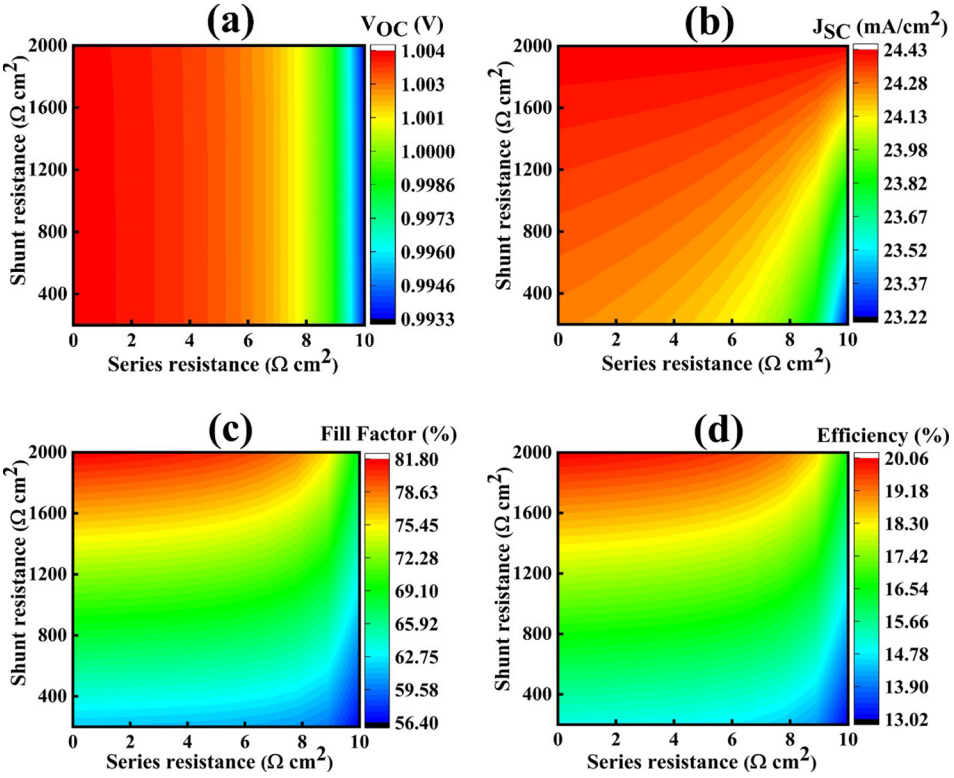


**Fig. 8.** (a–d) The effect of series and shunt resistance on the open circuit voltage ($V_{OC}$), short circuit current ($J_{SC}$), Fill Factor (FF) and Efficiency of the solar cell device for $Sb_2S_3$/ZnS combination.

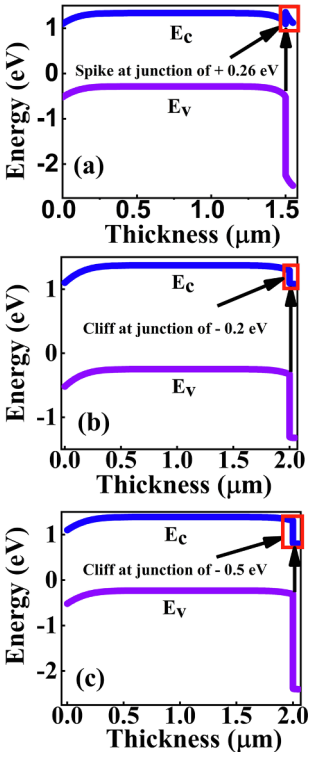


**Fig. 9.** The band diagram of the device structure and conduction band offset (CBO) at absorber/buffer counterpart interface. (a–c) represent device for $Sb_2S_3$/ZnS, $Sb_2S_3$/CdS and $Sb_2S_3$/$TiO_2$ combination respectively.

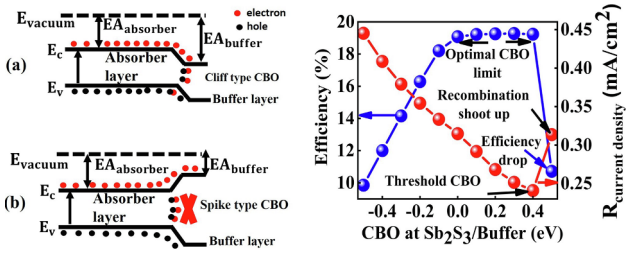


**Fig. 10.** (a–c) The schematic diagram of the cliff and spike type CBO at the absorber/buffer interface. (a) Shows that interfacial recombination is more favorable for cliff type junction and (b) shows that interfacial recombination is negligible for spike type junction. (c) Effect of CBO on the recombination current and efficiency of the solar device.

**Table 4**
The performance parameters of the device after level I optimizations.

| Structure | $V_{OC}$ (V) | $J_{SC}$(mA/cm$^2$) | FF (%) | Efficiency (%) | CBO (eV) |
|---|---|---|---|---|---|
| $Sb_2S_3$/$TiO_2$ | 0.6162 | 24.3100 | 64.79 | 9.71 | Cliff (−0.5 eV) |
| $Sb_2S_3$/CdS | 0.9180 | 24.3369 | 72.89 | 16.28 | Cliff (−0.2 eV) |
| $Sb_2S_3$/ZnS | 1.0027 | 24.399 | 78.31 | 19.16 | Spike (+0.26 eV) |
| $Sb_2Se_3$/CdS | 0.4114 | 40.8374 | 41.97 | 7.05 | Cliff (−0.2 eV) |

### 3.1.8. Simulation of $Sb_2Se_3$ as an absorber layer

We have also simulated selenide counterpart of $Sb_2S_3$ as an absorber, i.e.; $Sb_2Se_3$ absorber. Bandgap of $Sb_2(S_{1-x}Se_x)_3$ can be tuned from 1.08 eV (for x = 1) to 1.62 eV for x = 0). The optimum band gap of the absorber layer for single junction solar cell is in the range of ~1.3–1.4 eV. Therefore, we may check the efficiency for $Sb_2Se_3$ as absorber layer replacing $Sb_2S_3$ using buffer layers in the three configurations in the present studies. The simulated efficiency obtained for

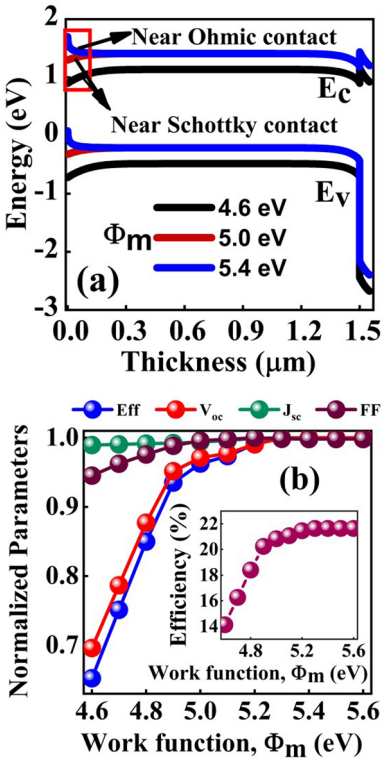


**Fig. 11.** (a) Effect of back contact metal work function on the band diagram of the device and shows how the near Schottky type junction changes to near Ohmic type junction depend on the back contact metal work function. (b) Effect of back contact metal work function on the performance of the solar device.

**Table 5**
The performance parameters of the device after optimizing back contact metal work function.

| Structure | $V_{OC}$ (V) | $J_{SC}$(mA/cm$^2$) | FF (%) | Efficiency (%) |
|---|---|---|---|---|
| $Sb_2S_3$/$TiO_2$ | 0.6410 | 24.4374 | 75.96 | 11.90 |
| $Sb_2S_3$/CdS | 0.9476 | 24.4393 | 79.96 | 18.52 |
| $Sb_2S_3$/ZnS | 1.0954 | 24.565 | 80.60 | 21.69 |

$Sb_2Se_3$/CdS configuration is 7.05%. The I-V curve and variation of performance parameters with metal work function is shown in Fig. S3 (a-b) and presented in Table 4. Its combination with other two buffer layers ($TiO_2$ and ZnS) could not converge. Clearly, the performance of $Sb_2Se_3$ absorber is poor in comparison to $Sb_2S_3$ absorber. However, it remains to be seen if partial substitution of sulphur with selenium can make any difference on solar cell performance. Such a feasibility has, in fact, been taken up in the level II of modeling in the present work.

In spite of the results and comparison described above, there are a number of factors that still require optimization to achieve further enhancement in efficiency. This has, in fact, been done in level II optimization, considering parameters such as high work function back contact metal and band gap grading of absorber layer for designing an optimally performing device structure. It is described in the next section.

### 3.2. Level II optimization

In this stage, the previously determining optimal parameters for each of the device structures in this study have been taken up for further optimization of back contact metal work function. At this stage, the best among the three was opted for band gap grading in the absorber aimed at maximum absorption for better conversion efficiency.

*3.2.1. Optimization of back contact metal work function*

The performance of SPV device drastically changes due to effect of back contact metal work function. Ideal requirement is Ohmic contact. Gold (Au) is widely used as back contact metal for the $Sb_2S_3$ solar cell. Back contact of $Sb_2Se_3$ with Au is nearly Ohmic. However, in $Sb_2S_3$ absorber, Au back contact creates Schottky type contact due to its p-type semiconducting property (Deng et al., 2017; Zhou et al., 2014). Therefore, majority carrier faces a barrier at the back contact thereby affecting collection charge carrier from the absorber ($Sb_2S_3$) layer. To overcome this, simulation has been performed on the $Sb_2S_3$ solar cell with varying work function of back contact metal in the range 4.6–5.6 eV retaining all other optimal parameters in this study fixed for all the device combinations. The quantity $(\varnothing_m - (E_g + \chi))$ is the factor of mismatch at the back junction, where $\varnothing_m$ is the metal work function, $E_g$ and $\chi$ are the band gap and electron affinity of the absorber layer respectively. To show the effect of back contact metal work function on band diagram $Sb_2S_3$/ZnS combination is opted and the results are shown in the Fig. 11 (a). It is seen in the Fig. 11 (a) the energy levels of absorber, bend upwards at the metal contact for the metal work function values in the range of 4.6–5.4 eV. This type of bending present a barrier for transport of hole while it energetically favors electron transporting towards back contact. As a results rate of recombination becomes large affecting device performance parameters adversely due to Schottky type contact formation. However, with back contact metal work function ~5.4 eV, there is the metal absorber contact exhibiting Ohmic contact response (Fig. 11 (a)). Such an energetically favorable alignment is optimum condition for solar cell structure to facilitate unidirectional flow of charge carriers in the device. The effect of back contact metal work function modification on device performance parameters is shown in the Fig. 11 (b) and also presented in Table 5. It is seen that $V_{OC}$ significantly depends on $\varnothing_m$ while $J_{SC}$ and FF has very little dependence on $\varnothing_m$. An optimal efficiency is obtained for back contact metal work function lying in the range of ~5.4–5.6 eV. Therefore, appropriate selection of back contact metal work function has great potential to enhance efficiency of solar cells. To meet this requirement, one has to focus on high work function metals such as Pt that, in turn, would bring higher cost as an implementation. Therefore, we need to look at alternative path or techniques to decrease the metal work function for optimum condition of the device. This issue has been addressed by adopting absorber layer band gap grading using suitable element without affecting lattice-matching condition. This is described in the following Section 3.2.2.

*3.2.2. Optimization of band gap grading of the absorber layer*

Considering optimal efficiency using high work function metal (Pt) as the back contact, the device structure $Sb_2S_3$/ZnS was opted for further optimization based on band gap grading approach. The variation of the ratio (x) ≅ Se/(Se + S), will affect the band gap according to relation; $E_g(x) = 0.118x^2 - 0.662x + 1.621$ eV where 0.118 eV was the bowing parameter (Yang et al., 2015). Vigil et al., 2018 have theoretically shown that a variation of the Se/(Se + S) would affect the level of valence band maximum. Therefore, such tailoring of energy band diagram creates an additional electric field ($\xi_A$) over the absorber layer, and can expressed as;

$$\xi_A = \frac{d\Delta E_g}{dx} \tag{6}$$

where $\Delta E_g$ is the band gap variation for the thickness (x) of the absorber layer due to Se grading. Carrier collection of photoelectrons generated outside the space charge region (SCR) in homogeneous $Sb_2S_3$ now depends only on diffusion. The charge carrier collection probability, $P_C$, outside the SCR is given by the Eq. (7)

$$P_C = e^{\frac{-x}{L_d}} \tag{7}$$

where x is the distance from the SCR and $L_d$ is the diffusion length. The increasing ratio of Se/(Se + S) sets up an additional force (or electric field) on the hole towards the back contact, this in turn effectively improves the carrier collection at the back contact. Further, the enhanced diffusion length due to effective electric field, L, can be expressed by the Eq. (8)

$$L = \mu_h \cdot \xi_A \cdot \tau_h = \frac{\xi_A}{kT/q} \cdot L_d^2 \tag{8}$$

$$\text{Using } L_d = (D_h \tau_h)^{1/2} \tag{9}$$

$$\text{we get; } = \mu_h \cdot kT/q \tag{10}$$

where, $\mu_h$ is the hole mobility, $\tau_h$ is the carrier lifetime, $D_h$ is the diffusion coefficient of hole, $k$ is the boltzman constant, T is the absolute temperature and q is the charge of electron (Lundberg et al., 2005). From the equation (8), it is clear that carrier collection will be significantly enhanced with the additional electric field obtained via Se grading. Here, it is also noticed that the additional length in the effective electric field is directly proportional to $L_d^2$. This means if a material has already long diffusion length without Se-grading then it will have much longer diffusion length after Se-grading. Consequently, the band diagram of the absorber layer on Se- grading in the $Sb_2S_3$ solar cell undergoes modification which is shown in the Fig. 12 (a–d). On enhancement of effective diffusion length of hole and unidirectional flow of charge carrier, the optical absorption automatically increases over a wide range shown schematically in the Fig. 13 (a). After implementing band gap grading based optimization, metal work function considering high cost of Pt as back contact variation for optimal efficiency was further investigated and the results is shown in Fig. 13 (b). It indicated an optimal efficiency ~25% obtained for a metal back contact over a range of metal work function ~5.1–5.3 eV which is compatible with a number of metals such as Au (4.8–5.1 eV), Mo (5.0–5.1 eV), Ni (4.8–5.1 eV). So, the cost barrier pertaining to use of Pt as metal back contact has been overcome with relatively cheaper alternatives and with enhanced efficiency. It is important to note at this stage that before selenium grading metal like (Au, Ni, and Mo) makes a Schottky contact at $Sb_2S_3$/metal junction. This was great hindrance for higher efficiency. Now, with band gap grading in place, metals like Au, Ni, and Mo makes a good Ohmic contact at Se-graded $Sb_2S_3$/metal junction. This is a noteworthy contribution of the present work and is an outcome of complete simulation implemented considering large spectrum of materials and design parameters. The final simulated results are presented in the Table 6. It is observed that the optimal band gap grading of the $Sb_2S_3$ absorber layer was noted for the ranges 1.31–1.62 eV. It is noted that the band gap grading enhanced efficiency obtained at level I optimization from 19.16% to 24.81% after completion of level II optimization with low work function metal for Ohmic contact. Therefore, it

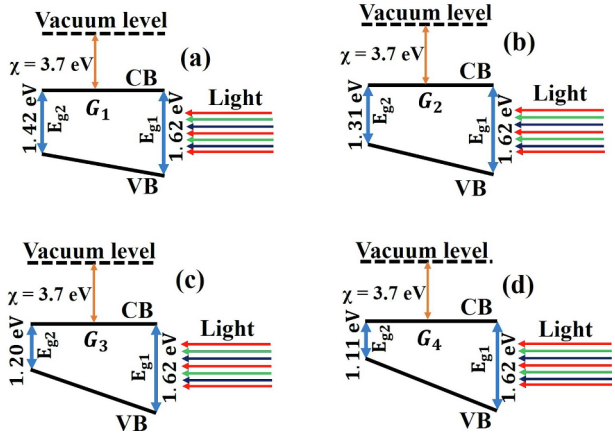


**Fig. 12. .** (a–d) The schematic band diagram of the different linear band gap grading of the absorber layer by varying Se/(Se + S) composition ratio.

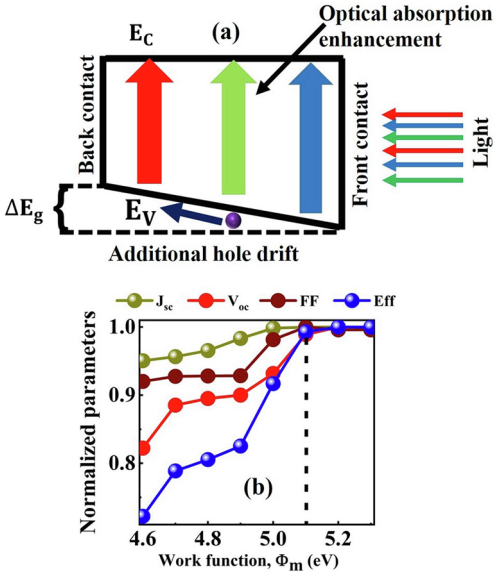


**Fig. 13. .** (a) Schematic diagram of the band gap grading of absorber layer shows that optical absorption and rate of carrier transporting enhances, (b) Effect of back contact metal work function on efficiency after band gap grading of the absorber layer.

**Table 6**
The performance parameters of the device after band gap grading of absorber layer.

| Graded solar device (Fig. 12) | $V_{OC}$ (V) | $J_{SC}$ (mA/cm$^2$) | FF (%) | Efficiency (%) |
|---|---|---|---|---|
| $G_1$ ($Sb_2(S_{.83}Se_{.17})_3$/ZnS) | 0.9986 | 28.80 | 81.67 | 23.49 |
| $G_2$ ($Sb_2(S_{.73}Se_{.27})_3$/ZnS) | 0.9656 | 31.70 | 81.03 | 24.81 |
| $G_3$ ($Sb_2(S_{.50}Se_{.50})_3$/ZnS) | 0.8957 | 34.36 | 79.84 | 24.57 |
| $G_4$ ($Sb_2(S_{.33}Se_{.67})_3$/ZnS) | 0.8206 | 36.50 | 78.79 | 23.60 |

is predicted in general, that efficiency will be higher for the mixed selenide and sulphur phase where the composition $Sb_2(S_{1-x}Se_x)_3$ is such that the bandgap attain an optimal value (~1.3–1.4 eV). So, bandgap grading can be exploited as a tool to tune absorption ability of $Sb_2S_3$ delivering an optimum performance as a solar cell structure.

### *3.2.3. Optimization of SPV performance Vis-a vis temperature*

In this section, we have discussed the effect of temperature on the optimized solar cell discussed above. The effect of temperature has been performed by keeping other optimal parameters fixed in the range of 270 K to 380 K. The variation of performance parameters estimated in terms of open circuit voltage ($V_{OC}$), short circuit current ($J_{SC}$), Fill Factor (FF) and efficiency (η) with variation of temperature has been shown in the Fig. S4 (a–d). The energy of the electron increases with increase of temperature due to corresponding lowering of effective band gap of semiconductor. However, the electrons with excessive energy at high temperatures augments recombination with hole thereby creating recombination current (Green, 2003). It was observed from Fig. S4 (a) that $V_{OC}$ significantly decreases with temperature because reverse saturation current increases with increase of temperature. The effect of temperature on $J_{SC}$ is not significant like $V_{OC}$. The fill factor (FF) decreases linearly with temperature due to light-induced degradation shown in Fig. S4 (c) (Green, 2003). It is clear from Fig. S4 (d) that the efficiency of the device decreases linearly with temperature because of combined effect of temperature on $V_{OC}$, $J_{SC}$ and FF. Further, it was observed that at temperatures below 300 K, efficiency is stable and becomes maximum ~26.59% at 270 K. So, the ideal range of temperature, for best performance as per prediction here in this work, may be 20–25 °C as expected.

## 4. Summary and Conclusion

In this work, we have undertaken experimentally reported $Sb_2S_3$/buffer layer (like CdS, $TiO_2$) heterojunction solar cell configuration and attempted to analyze the primary reasons for its lower efficiency. It came to our notice that the low experimental efficiency traces its origin to unoptimised band alignment at the $Sb_2S_3$/buffer layer junction and formation of Schottky contact at the $Sb_2S_3$/metal junction. Subsequently, performance optimization was taken up by focusing on suitable choice of back contact metal work function, band gap grading of the $Sb_2S_3$ absorber layer and a spike-type band alignment at the $Sb_2S_3$/buffer layer junction. In our simulation results, it was noted that spike-type band alignment at the front contact and high work function metal at the back contact are essential requirements to enhance device performance. We also introduced an additional concept of band gap grading to lower the high work function at metal back contact and demonstrated an increase in device efficiency at the end of 2nd level design optimization. With these modifications, the efficiency of $Sb_2S_3$/ZnS solar cell was predicted to be 24.81%, which is almost comparable to the conventional thin film solar cell. The results confirmed that the desired optimal architecture of the $Sb_2S_3$ absorber based solar cell must comprise metal back contact with work function ~5.1 eV (e.g. Ni, Mo), absorber band gap grading in the range 1.31–1.62 eV (varying the ratio of Se/ (Se + S)), with CBO of 0.26 eV between absorber $Sb_2S_3$ and buffer layer (ZnS).

It is concluded that out of the three solar cell configurations comprising $Sb_2S_3$ absorber and 3 different buffer layers ($TiO_2$, CdS and ZnS), the optimal configuration in terms of performance yielding a spike-type band alignment at conduction band of $Sb_2S_3$/buffer junction is achievable in ZnS buffer. So, it can be a replacement for CdS and $TiO_2$ in optimal experimental design.

## Declaration of Competing Interest

The authors declare that they have no known competing financial interests or personal relationships that could have appeared to influence the work reported in this paper.

## Acknowledgement

Author Mr. M.T. Islam, DST INSPIRE Fellow (IF160324), is grateful to DST for financial assistance, gratefully acknowledge Dr. Marc Burgelman, Honorary Professor, University of Gent for providing open source SCAPS-1D software and Atul Kumar, Research scholar Physics department IIT Patna, for discussion during the course of manuscript preparation.

## Appendix A. Supplementary data

Supplementary data to this article can be found online at https://doi.org/10.1016/j.solener.2020.03.058.

## References

Ahn, Y.H., Park, J.Y., Lee, S., Ryu, S., Nguyen, D.C., Ha, Na Young, Park, H.J., 2016. Hole-extraction layer dependence of defect formation and operation of planar $CH_3NH_3PbI_3$ perovskite solar cells. Phys. Status Solidi - Rapid Res. Lett. 11, 1–5. https://doi.org/10.1002/pssr.201600395.

Bauer, A., Sharbati, S., Powalla, M., 2017. Solar Energy Materials & Solar Cells Systematic survey of suitable buffer and high resistive window layer materials in $CuIn_{1-x}Ga_xSe_2$ solar cells by numerical simulations. Sol. Energy Mater. Sol. Cells. 165, 119–127. https://doi.org/10.1016/j.solmat.2016.12.035.

Burgelman, M., Decock, K., Khelifi, S., Abass, A., 2013. Advanced electrical simulation of thin film solar cells. Thin Solid Films. 535, 296–301. https://doi.org/10.1016/j.tsf.2012.10.032.

Burgelman, M., Nollet, P., Degrave, S., 2000. Modelling polycrystalline semiconductor solar cells. Thin Solid Films. 361, 527–532. https://doi.org/10.1016/S0040-6090(99)00825-1.

Chen, X., Li, Z., Zhu, H., Wang, Y., Liang, B., Chen, J., Xu, Y., Mai, Y., 2017. CdS/$Sb_2S_3$

heterojunction thin film solar cells with a thermally evaporated absorber. J. Mater. Chem. C. 5, 9421–9428. https://doi.org/10.1039/c7tc02460f.
Choi, Y.C., Lee, D.U., Noh, J.H., Kim, E.K., Seok II, S., 2014. Highly improved $Sb_2S_3$ sensitized-inorganic-organic heterojunction solar cells and quantification of traps by deep-level transient spectroscopy. Adv. Funct. Mater. 24, 3587–3592. https://doi.org/10.1002/adfm.201304238.
Courel, M., Jiménez, T., Arce-Plaza, A., Seuret-Jiménez, D., Morán-Lázaro, J.P., Sánchez-Rodríguez, F.J., 2019. A theoretical study on Sb2S3 solar cells: The path to overcome the efficiency barrier of 8%. Sol. Energy Mater. Sol. Cells. 201, 110–123. https://doi.org/10.1016/j.solmat.2019.110123.
Decock, K., Zabierowski, P., Burgelman, M., 2012. Modeling metastabilities in chalcopyrite-based thin film solar cells. J. Appl. Phys. 111. https://doi.org/10.1063/1.3686651.
Deng, H., Yuan, S., Yang, X., Cai, F., Hu, C., Qiao, K., Zhang, J., Tang, J., Song, H., He, Z., 2017. Efficient and stable $TiO_2/Sb_2S_3$ planar solar cells from absorber crystallization and Se-atmosphere annealing. Mater. Today Energy. 3, 15–23. https://doi.org/10.1016/j.mtener.2017.02.001.
Deng, H., Zeng, Y., Ishaq, M., Yuan, S., Zhang, H., Yang, X., Hou, M., Farooq, U., Huang, J., Sun, K., Webster, R., Wu, H., Chen, Z., Yi, F., Song, H., Hao, X., Tang, J., 2019. Quasiepitaxy Strategy for Efficient Full-Inorganic $Sb_2S_3$ Solar Cells. Adv. Funct. Mater. 1901720, 1–10. https://doi.org/10.1002/adfm.201901720.
El-Sayad, E.A., 2008. Compositional dependence of the optical properties of amorphous $Sb_2Se_{3-x}S_x$ thin films. J. Non. Cryst. Solids. 354, 3806–3811. https://doi.org/10.1016/j.jnoncrysol.2008.05.004.
Escorcia-García, J., Becerra, D., Nair, M.T.S., Nair, P.K., 2014. Heterojunction $CdS/Sb_2S_3$ solar cells using antimony sulfide thin films prepared by thermal evaporation. Thin Solid Films. 569, 28–34. https://doi.org/10.1016/j.tsf.2014.08.024.
Giraldo, S., Jehl, Z., Placidi, M., Izquierdo-roca, V., Pérez-rodríguez, A., Saucedo, E., Field, C.P., 2019. Progress and Perspectives of Thin Film Kesterite Photovoltaic Technology : A Critical Review. Adv. Mater. 31, 1806692. https://doi.org/10.1002/adma.201806692.
Gödel, K.C., Choi, Y.C., Roose, B., Sadhanala, A., Snaith, H.J., Seok II, S., Steiner, U., Pathak, S.K., 2015. Efficient room temperature aqueous $Sb_2S_3$ synthesis for inorganic-organic sensitized solar cells with 5.1% efficiencies. Chem. Commun. 51, 8640–8643. https://doi.org/10.1039/c5cc01966d.
Green, M.A., 1984. Limits on the open-circuit voltage and efficiency of silicon solar cells imposed by intrinsic auger processes. IEEE Trans. Electron Dev., ED-31, 5.
Green, M.A., 2003. General temperature dependence of solar cell performance and implications for device modelling. Prog. Photovoltaics Res. Appl. 11, 333–340. https://doi.org/10.1002/pip.496.
Green, M.A., Yoshita, M., Dunlop, E.D., Levi, D.H., Baillie, A.W.Y.H., 2019. Solar cell efficiency tables (version 54). Prog Photovolt Res Appl. 27, 565–575. https://doi.org/10.1002/pip.3171.
Haddout, A., Fahoume, M., Qachaou, A., Raidou, A., Lharch, M., Elharfaoui, N., 2019. Influence of composition ratio on the performances of kesterite solar cell with double CZTS layers—A numerical approach. Sol. Energy. 189, 491–502. https://doi.org/10.1016/j.solener.2019.07.098.
Heise, S.J., Gerliz, V., Hammer, M.S., Ohland, J., Keller, J., 2017. Light-induced changes in the minority carrier di ff usion length of Cu(In, Ga)$S_e$2 absorber material. Sol. Energy Mater. Sol. Cells. 163, 270–276. https://doi.org/10.1016/j.solmat.2017.01.045.
Huang, S., Luo, W., Zou, Z., 2013. Band positions and photoelectrochemical properties of $Cu_2ZnSnS_4$ thin films by the ultrasonic spray pyrolysis method. J. Phys. D. Appl. Phys. 46, 235108. https://doi.org/10.1088/0022-3727/46/23/235108.
Im, S.H., Lim, C.S., Chang, J.A., Lee, Y.H., Maiti, N., Kim, H.J., Nazeeruddin, M.K., Grätzel, M., Seok II, S., 2011. Toward interaction of sensitizer and functional moieties in hole-transporting materials for efficient semiconductor-sensitized solar cells. Nano Letters 11, 4789–4793. https://doi.org/10.1021/nl2026184.
Jackson, P., Hariskos, D., Lotter, E., Paetel, S., Wuerz, R., Menner, R., Wischmann, W., Powalla, M., 2011. New world record efficiency for Cu(In, Ga)$S_e$2 thin-film solar cells beyond 20%. Prog. Photovolt: Res. Appl. 19, 894–897. https://doi.org/10.1002/pip.
Kamruzzaman, M., Chaoping, L., Yishu, F., Farid Ul Islam, A.K.M., Zapien, J.A., 2016. Atmospheric annealing effect on TiO2/Sb2S3/P3HT heterojunction hybrid solar cell performance. RSC Adv. 6, 99282–99290. https://doi.org/10.1039/c6ra20378g.
Kanoun, A.A., Kanoun, M.B., Merad, A.E., Goumri-Said, S., 2019. Toward development of high-performance perovskite solar cells based on $CH_3NH_3GeI_3$ using computational approach. Sol. Energy 182, 237–244. https://doi.org/10.1016/j.solener.2019.02.041.
Khattak, Y.H., Baig, F., Soucase, B.M., Beg, S., Gillani, S.R., Ahmed, S., 2018. Efficiency enhancement of novel CNTS/ZnS/Zn (O, S) thin film solar cell. Optik (Stuttg) 171, 453–462. https://doi.org/10.1016/j.ijleo.2018.06.001.
Kim, D.H., Lee, S.J., Park, M.S., Kang, J.K., Heo, J.H., Im, S.H., Sung, S.J., 2014. Highly reproducible planar $Sb_2S_3$-sensitized solar cells based on atomic layer deposition. Nanoscale 6, 14549–14554. https://doi.org/10.1039/c4nr04148h.
Kondrotas, R., Chen, C., Tang, J., 2018. $Sb_2S_3$ Solar Cells. Joule 2, 857–878. https://doi.org/10.1016/j.joule.2018.04.003.
Kumar, A., Thakur, A.D., 2018. Role of contact work function, back surface field, and conduction band offset in $Cu_2ZnSnS_4$ solar cell. Jpn. J. Appl. Phys. 57, 08RC05. https://doi.org/10.7567/JJAP.57.08RC05.
Lamb, D.A., Baker, M.A., Underwood, C.I., Irvine, S.J.C., Barrioz, V., Gwilliam, R., Hall, J., 2017. Proton irradiation of CdTe thin film photovoltaics deposited on cerium - doped space glass. Prog. Photovolt. Res. Appl. 25, 1059–1067. https://doi.org/10.1002/pip.2923.
Li, Z., Liang, X., Li, G., Liu, H., Zhang, H., Guo, J., Chen, J., Shen, K., San, X., Yu, W., Schropp, R.E.I., Mai, Y., 2019. 9.2%-efficient core-shell structured antimony selenide nanorod array solar cells. Nat. Commun. 1–9. https://doi.org/10.1038/s41467-018-07903-6.
Lin, L. yan, Jiang, L. qin, Qiu, Y., Fan, B. dian, 2018. Analysis of Sb2Se3/CdS based photovoltaic cell: A numerical simulation approach. J. Phys. Chem. Solids. 122, 19–24. http://doi.org/10.1016/j.jpcs.2018.05.045.
Lundberg, O., Edoff, M., Stolt, L., 2005. The effect of Ga-grading in CIGS thin film solar cells. Thin Solid Films. 480–481, 520–525. https://doi.org/10.1016/j.tsf.2004.11.080.
Schleussner, S.M., Pettersson, J., Törndahl, T., Edoff, M., 2013. Surface engineering in Cu (In, Ga)$S_e$2 solar cells. Prog. Photovolt: Res. Appl. 21, 561–568. https://doi.org/10.1002/pip.
Tamilselvan, M., Byregowda, A., Su, C.-Y., Tseng, C.-J., Bhattacharyya, A.J., 2019. Planar Heterojunction Solar Cell Employing a Single-Source Precursor Solution-Processed $Sb_2S_3$ Thin Film as the Light Absorber. ACS Omega 4, 11380–11387. https://doi.org/10.1021/acsomega.9b01245.
Thalía, Jiménez, León-Pimentel, C.I., Seuret-Jiménez, D., Courel, M., 2019. State of the Art on $Sb_2(S_{1-x}Se_x)_3$ Thin Film Solar CellsState of the Art on $Sb_2(S_{1-x}Se_x)_3$ Thin Film Solar Cells. Gen. Chem. Chem. Chem. 5https://doi.org/10.21127/yaoyigc20180029.180029-180029.
Tiedje, T.O.M., Yablonovitch, E.L.I., Cody, G.D., Brooks, B.G., 1984. Limiting Efficiency of Silicon Solar cells. IEEE Trans. Electron Dev. ED-31 (5), 711–716.
Tumelero, M.A., Faccio, R., Pasa, A.A., 2016. Unraveling the native conduction of trichalcogenides and its ideal band alignment for new photovoltaic interfaces. J. Phys. Chem. C. 120, 1390–1399. https://doi.org/10.1021/acs.jpcc.5b10233.
Vigil-Galán, O., Jiménez, T., Seuret-Jiménez, D., Basurto-Pensado, M.A., Courel, M., 2018. Sb2(S1 − xSex)3 solar cells: the impact of radiative and non-radiative loss mechanisms. J. Phys. D: Appl. Phys. 51, 435501 (12pp).
Wang, K., Cheng, J., Yang, X., Hu, R., Fu, L., Huang, J., Yu, J., Li, L., 2018a. Enhanced Photovoltaic Properties in $Sb_2S_3$ Planar Heterojunction Solar Cell with a Fast Selenylation Approach. Nanoscale Res. Lett. 13. https://doi.org/10.1186/s11671-018-2651-x.
Wang, R., Mujahid, M., Duan, Y., Wang, Z.K., Xue, J., Yang, Y., 2019a. A Review of Perovskites Solar Cell Stability. Adv. Funct. Mater. 1808843, 1–25. https://doi.org/10.1002/adfm.201808843.
Wang, X., Li, J., Liu, W., Yang, S., Zhu, C., Chen, T., 2017. A fast chemical approach towards Sb 2 S 3 film with a large grain size for high-performance planar heterojunction solar cells. Nanoscale 9, 3386–3390. https://doi.org/10.1039/c7nr00154.
Wang, X., Tang, R., Wu, C., Zhu, C., Chen, T., 2018b. Development of antimony sulfide–selenide $Sb_2(S, Se_)3$-based solar cells. J. Energy Chem. 27, 713–721. https://doi.org/10.1016/j.jechem.2017.09.031.
Wang, X., Tang, R., Yin, Y., Ju, H., Li, S., Zhu, C., Chen, T., 2019b. Interfacial engineering for high efficiency solution processed $Sb_2Se_3$ solar cells. Sol. Energy Mater. Sol. Cells 189, 5–10. https://doi.org/10.1016/j.solmat.2018.09.020.
Wei, S.Y., Liao, Y.C., Hsu, C.H., Cai, C.H., Huang, W.C., Huang, M.C., Lai, C.H., 2016. Achieving high efficiency $Cu_2ZnSn(S, Se_)4$ solar cells by non-toxic aqueous ink : Defect analysis and electrical modeling. Nano Energy 26, 74–82. https://doi.org/10.1016/j.nanoen.2016.04.059.
Wu, C., Jiang, C., Wang, X., Ding, H., Ju, H., Zhang, L., Chen, T., Zhu, C., 2019. Interfacial Engineering by Indium-Doped CdS for High Efficiency Solution Processed $Sb_2(S_{1-x}Se_x)_3$ Solar Cells. ACS Appl. Mater. Interfaces 11, 3207–3213. https://doi.org/10.1021/acsami.8b18330.
Yang, B., Xue, D.J., Leng, M., Zhong, J., Wang, L., Song, H., Zhou, Y., Tang, J., 2015. Hydrazine solution processed $Sb_2S_3$, $Sb_2Se_3$ and $Sb_2(S_{1-x}Se_x)_3$ film: molecular precursor identification, film fabrication and band gap tuning. Sci. Rep. 5, 1–11. https://doi.org/10.1038/srep10978.
You, M.S., Lim, C.S., Kwon, D.H., Heo, J.H., Im, S.H., Chae, K.J., 2015. Oxide-free $Sb_2S_3$ sensitized solar cells fabricated by spin and heat-treatment of Sb(III) $(thioacetamide)_2Cl_3$. Org. Electron. Phys. Mater. Appl. 21, 155–159. https://doi.org/10.1016/j.orgel.2015.02.015.
Yuan, S., Deng, H., Dong, D., Yang, X., Qiao, K., Hu, C., Song, Huaibing, Song, Haisheng, He, Z., Tang, J., 2016. Efficient planar antimony sulfide thin film photovoltaics with large grain and preferential growth. Sol. Energy Mater. Sol. Cells 157, 887–893. https://doi.org/10.1016/j.solmat.2016.07.050.
Yuan, S., Deng, H., Yang, X., Hu, C., Khan, J., Ye, W., Tang, J., Song, H., 2017. Postsurface Selenization for High Performance $Sb_2S_3$ Planar Thin Film Solar Cells. ACS Photonoics 11, 2862–2870. https://doi.org/10.1021/acsphotonics.7b00858.
Zhou, Y., Leng, M., Xia, Z., Zhong, J., Song, H., Liu, X., Yang, B., Zhang, J., Chen, J., Zhou, K., Han, J., Cheng, Y., Tang, J., 2014. Solution-processed antimony selenide heterojunction solar cells. Adv. Energy Mater. 4, 4–11. https://doi.org/10.1002/aenm.201301846.
Zimmermann, E., Pfadler, T., Kalb, J., Dorman, J.A., Sommer, D., Hahn, G., Weickert, J., Schmidt-Mende, L., 2015. Toward High-Efficiency Solution-Processed Planar Heterojunction $Sb_2S_3$ Solar Cells. Adv. Sci. 2, 1500059. https://doi.org/10.1002/advs.201500059.